



Article

# Fracture Mechanisms of Electrothermally Fatigued 631 Stainless Steel Fine Wires for Probe Spring Applications

Chien-Te Huang, Fei-Yi Hung \* and Kai-Chieh Chang

Department of Materials Science and Engineering, National Cheng Kung University, No. 1, Daxue Rd., East Dist., Tainan City 70101, Taiwan

\* Correspondence: fyhung@mail.ncku.edu.tw

#### **Abstract**

This study systematically investigates 50  $\mu$ m-diameter 631 stainless steel fine wires subjected to both sequential and simultaneous electrothermomechanical loading to simulate probe spring conditions in microelectronic test environments. Under cyclic current loading (~ $10^4$  A/cm²), the 50  $\mu$ m 631SS wire maintained electrical integrity up to 0.30 A for 15,000 cycles. Above 0.35 A, rapid oxide growth and abnormal grain coarsening resulted in surface embrittlement and mechanical degradation. Current-assisted tensile testing revealed a transition from recovery-dominated behavior at  $\leq$ 0.20 A to significant thermal softening and ductility loss at  $\geq$ 0.25 A, corresponding to a threshold temperature of approximately 200 °C. These results establish the endurance limit of 631 stainless steel wire under coupled thermal–mechanical–electrical stress and clarify the roles of Joule heating, oxidation, and microstructural evolution in electrical fatigue resistance. A degradation map is proposed to inform design margins and operational constraints for fatigue-tolerant, electrically stable interconnects in high-reliability probe spring applications.

**Keywords:** 631 (17-7PH) stainless steel; fine wire; electrical fatigue; electrothermal effect; probe spring



Academic Editors: Abílio M. P. De Jesus, Andrea Carpinteri, Jesús Toribio, Pejo Konjatić and Marko Katinić

Received: 16 June 2025 Revised: 18 July 2025 Accepted: 23 July 2025 Published: 1 August 2025

Citation: Huang, C.-T.; Hung, F.-Y.; Chang, K.-C. Fracture Mechanisms of Electrothermally Fatigued 631 Stainless Steel Fine Wires for Probe Spring Applications. *Appl. Sci.* **2025**, 15, 8572. https://doi.org/10.3390/ app15158572

Copyright: © 2025 by the authors. Licensee MDPI, Basel, Switzerland. This article is an open access article distributed under the terms and conditions of the Creative Commons Attribution (CC BY) license (https://creativecommons.org/licenses/by/4.0/).

#### 1. Introduction

Probe springs provide compliant electrical contact in automated test platforms, lab-on-a-chip devices, and semiconductor packaging systems, demanding reliable performance under combined thermal and mechanical stress [1,2]. As testing complexity increases, operational reliability becomes crucial to ensure signal integrity, minimize test errors, and reduce downtime and failures associated with thermal softening or contact resistance instability, which can directly impair production yield and equipment efficiency [3].

Conventional probe springs, typically fabricated from gold-coated alloy (50  $\mu$ m diameter), exhibit limited wear resistance and mechanical stability under repeated contact [4,5]. More critically, when subjected to high-frequency currents (current densities >  $10^4$  A/cm²), these wires undergo severe electrothermal degradation. This degradation is governed by four primary mechanisms [6–8]: (1) Joule heating, inducing local temperature increase and thermal fatigue; (2) residual stress relaxation, reducing elastic recovery; (3) electromigration, accumulating and voiding atomic vacancy; and (4) surface oxidation, impairing electrical conduction and introducing interfacial instability. These processes collectively undermine long-term reliability in high-cycle testing environments. Impulse-loading studies on MEMS metallic films further demonstrate that oxidation-assisted cracking can dominate

failure even at submillisecond timescales, highlighting the need for oxidation-resistant conductors [9].

Precipitation-hardened duplex stainless steels, particularly AISI 631 (17-7PH), offer a promising pathway for enhanced spring probe performance. The 631SS features thermally stable nanoscale B2–NiAl and Ni<sub>3</sub>Al precipitates, which provide high yield strength (~1.1 GPa), wear, corrosion, fatigue resistance, and oxidation tolerance at elevated temperatures [10–13]. These precipitates act as barriers to dislocation motion, helping to suppress grain coarsening. While bulk properties of 631SS are well documented, the electromechanical reliability of fine wires ( $\emptyset \approx 50~\mu m$ ) under electrical fatigue remains poorly understood. Early batch-mode, microelectro-discharge machining experiments revealed that microscale conductors suffer rapid surface degradation and conductivity loss when exposed to repetitive, high-density current pulses, yet a systematic link to duplex stainless steel wires is lacking [14]. Notably, the impact of such conditions on microstructure, oxide evolution, and failure behavior is insufficiently addressed in the current literature [15–18].

This study presents a systematic investigation of degradation mechanisms in cold-drawn 631 stainless steel fine wire under cyclic electrical loading, with emphasis on thermal fatigue cracking, electrothermal softening, and surface oxidation. Through combined microstructural and property-based analyses, this work aims to establish performance limits and design criteria for high-reliability, high-cycle probe spring applications. The findings provide both mechanistic insight and practical guidance for next-generation ATE and semiconductor test systems.

#### 2. Materials and Methods

#### 2.1. Material and Wire Drawing

631SS (17-7PH) precipitation-hardenable duplex stainless steel wire with an initial diameter of 0.75 mm was cold-drawn to a final diameter of 50  $\mu$ m, corresponding to a true strain of 99.56% (Figure 1a). The as-drawn wire is referred to as "As". All samples were prepared with a length of 50 mm. Figure 1b illustrates a schematic diagram depicting the operation of an electrically charged spring probe.

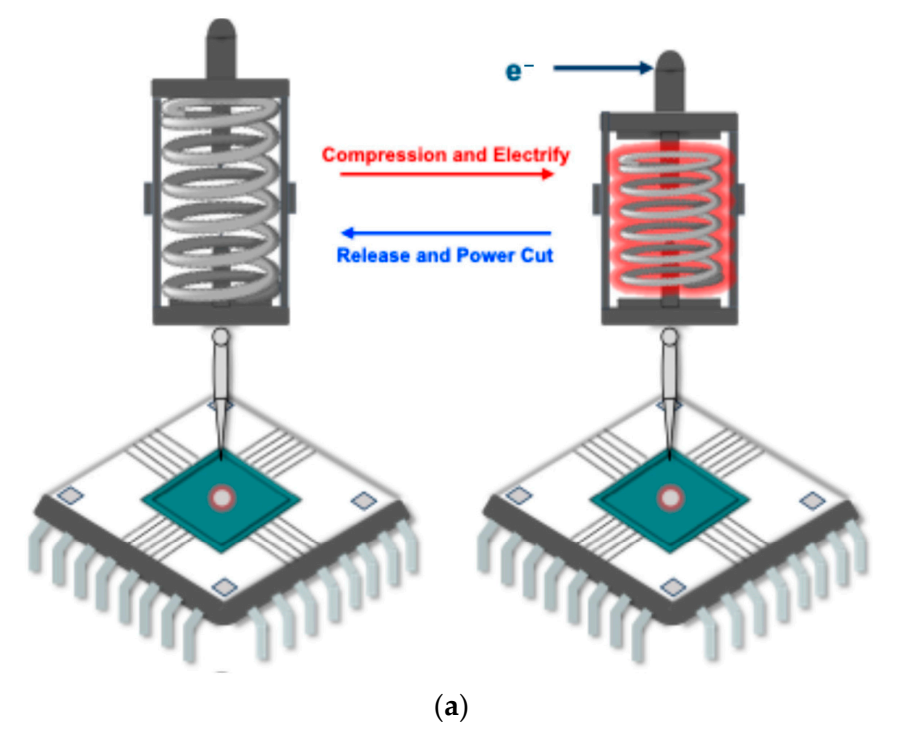
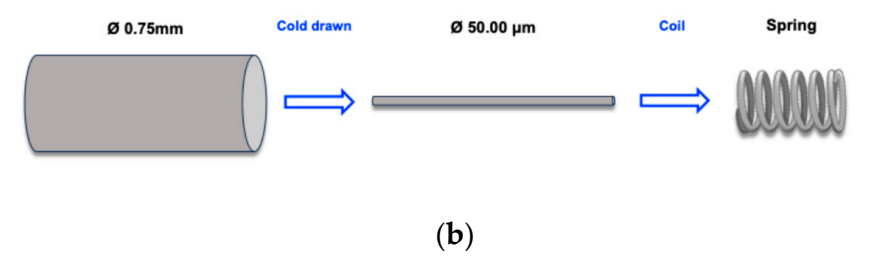


Figure 1. Cont.

Appl. Sci. 2025, 15, 8572 3 of 24



**Figure 1.** (a) Schematic of cold drawing and spring forming; (b) schematic diagram of electrically charged spring probe.

This figure illustrates the cyclic operation of the spring probe during the testing process:

- (1) Compression and current flow (red arrow), where electrical contact is established during compression, accompanied by Joule heating effects.
- (2) Release and power-off (blue arrow), where contact is broken and the current is disconnected during release.

This research assesses the mechanical performance, microstructure, and electrical fatigue life of the wire under varying current and cycle numbers through multiple and combined experiments. The experiments included microstructural analysis, Vickers hardness testing (HM-101, Mitutoyo, Taipei, Taiwan; 100 g load, 10 s dwell time), I–V characterization, standard tensile tests, and current-assisted tensile tests. Electrical fatigue life tests and fracture surface analysis were also performed to evaluate the effects of current magnitude and cycling number on mechanical degradation [19,20]. All experiments were independently repeated five times (n = 5). The reported data in all figures represent the mean values, with error bars indicating  $\pm 1$  standard deviation. Table 1 lists the calculated wire average temperatures, determined with Chang's empirical relation  $T(^{\circ}C) = \frac{I \times V}{0.00612} + 25$  [21]. The coupled electrical–mechanical experiments, therefore, probe spring tensile behavior from  $\approx 63 \, ^{\circ}C$  (0.10 A) to  $\approx 445 \, ^{\circ}C$  (0.30 A), a range spanning recovery, static recrystallization, and thermal softening regions.

**Table 1.** Electrothermal simulation under varying current levels and current densities.

Current (A)	0.00	0.10	0.20	0.25	0.30	0.35	0.37	0.39	0.41
J (A/ cm <sup>2</sup> )	0.00	$5.09 \times 10^{3}$	$1.02 \times 10^{4}$	$1.27\times10^4$	$1.53 \times 10^{4}$	$1.78 \times 10^{4}$	$1.88 \times 10^{4}$	$1.99 \times 10^{4}$	$2.09 \times 10^{4}$
Temp. (°C)	25	43-83	182–222	288–328	425–465	594-634	675–715	770-810	840–880

#### 2.2. Electrical Characterization and Electrical Fatigue Method (EFM)

The experimental setup for measuring the I–V characteristic, resistance, and electrical fatigue method (EFM) is shown in Figure 2. For all electrical tests, the wire length was fixed at 50 mm. Current–voltage (I–V) measurements were conducted by incrementally increasing the current from 0.00 A to 0.40 A in 0.05 A steps, followed by 0.01 A increments beyond 0.40 A until electrical fusing occurred. The fusing current ( $I_{fuse}$ ) was recorded, and dynamic resistance was calculated by applying Ohm's law within the linear region of the I–V curve.

Appl. Sci. 2025, 15, 8572 4 of 24

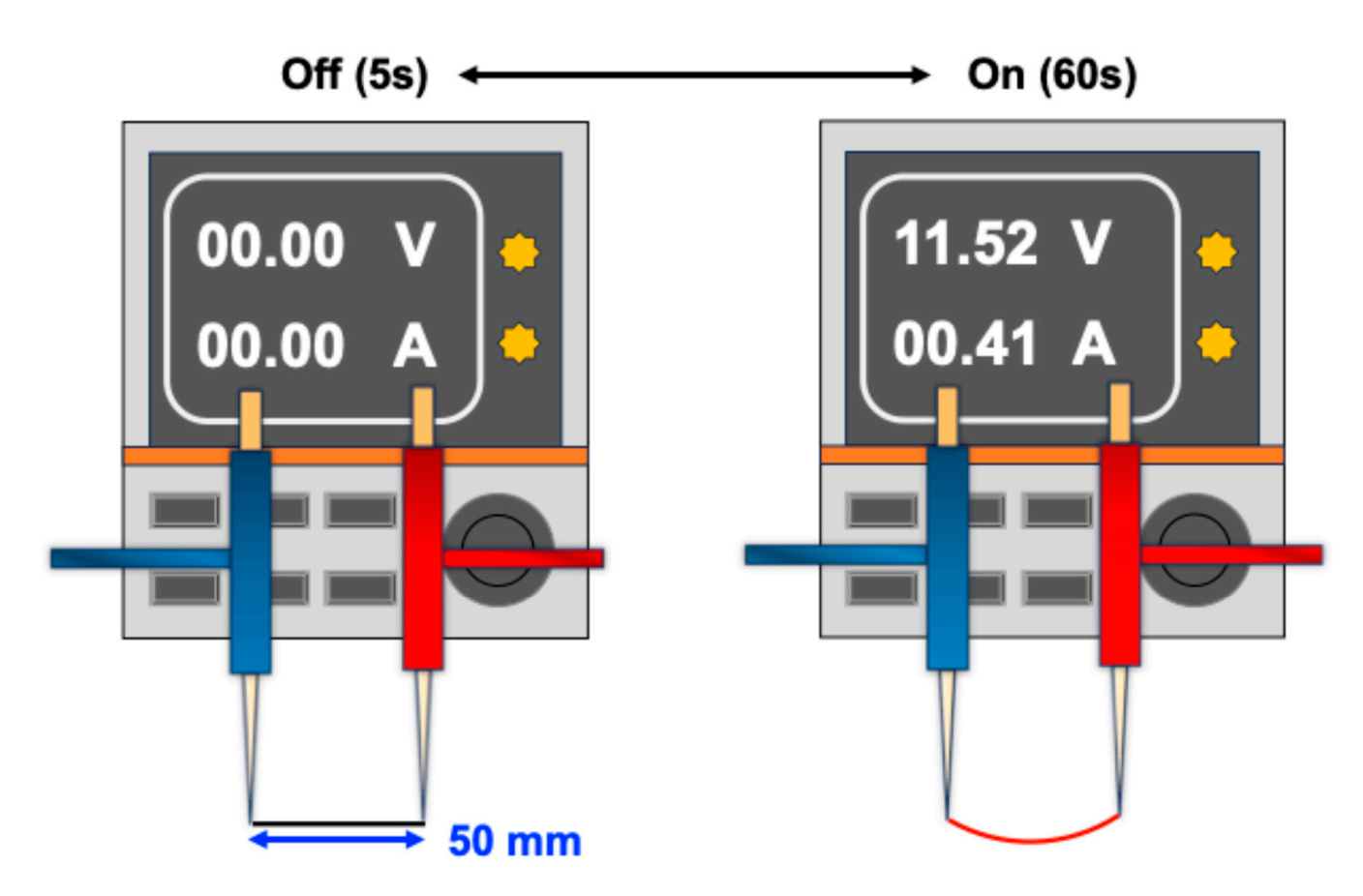


**Figure 2.** Schematic of the setup to measure I–V characteristics and the electrical fatigue method (EFM).

The electrical fatigue method (EFM) was implemented by applying intermittent direct current to wire specimens clamped at a 50 mm length. Each current period consisted of a 60-s ON and 5-s OFF cycle. The applied current levels were 0.30, 0.35, 0.37, 0.39, 0.41, 0.45, and 0.47 A. For each condition, the number of cycles to failure was recorded. Fracture morphology and surface features were subsequently examined using scanning electron microscopy (SEM, SU-5000, Hitachi, Tokyo, Japan).

# 2.3. Simulation Experiment of Probe Spring Operation

The tensile testing apparatus for the wire is depicted in Figure 3a. Uniaxial tensile tests were performed under displacement-controlled mode using constant crosshead speeds of 15, 30, 45, and 60 mm/min, corresponding to nominal engineering strain rates ( $\dot{\epsilon}$ ) of  $5.0 \times 10^{-3}$ ,  $1.0 \times 10^{-2}$ ,  $1.5 \times 10^{-2}$ , and  $2.0 \times 10^{-2}$  s<sup>-1</sup>, respectively. The engineering strain was calculated where  $L_0 = 50$  mm. The configuration for the current-assisted tensile test is shown in Figure 3b. Current-assisted tensile tests were performed on as-received 631 stainless steel wire under ambient conditions to evaluate the effects of simultaneous mechanical loading and electrical current. Tests were conducted at an engineering strain rate of  $5.0 \times 10^{-3}$  s<sup>-1</sup>, with current levels of 0.00, 0.10, 0.20, 0.25, and 0.30 A. Higher current levels were excluded as they induced immediate fracture upon tensile loading, precluding meaningful mechanical characterization. The objective was to simulate the mechanical electrical-thermal coupling encountered during spring operation in functional applications.

Appl. Sci. 2025, 15, 8572 5 of 24

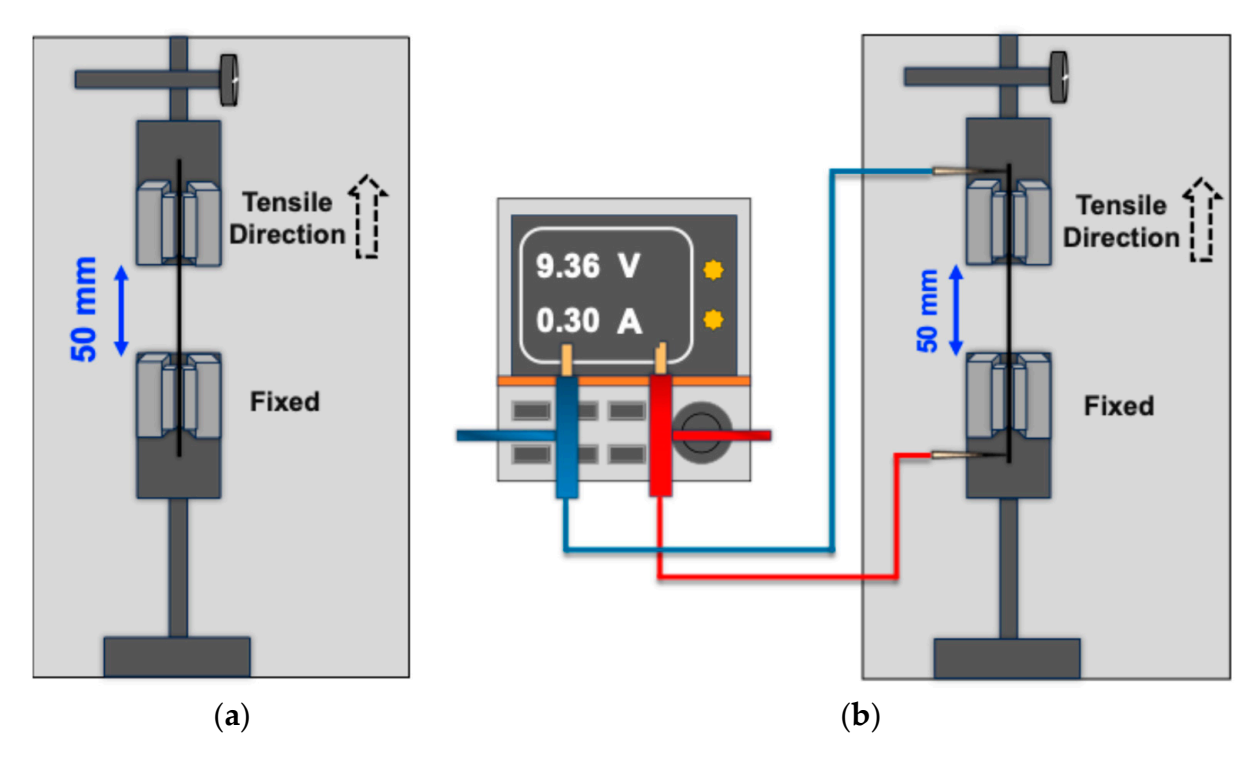


**Figure 3.** Experimental procedures: (a) Schematic of the setup for tensile testing; (b) schematic of the setup for current-assisted tensile test.

To replicate application-relevant electrothermal fatigue conditions, tensile tests were conducted on specimens previously subjected to electrical fatigue cycling (referred to as electrical fatigue tensile failure tests). All tests were performed under displacement control at an engineering strain rate of  $5.0 \times 10^{-3}~\rm s^{-1}$  to evaluate tensile properties, assess changes in I–V behavior, and characterize microstructural degradation. Each fatigued specimen was labeled using a "current–cycle" naming convention (e.g., 0.37-C100 denotes 0.37 A applied for 100 cycles).

Electrical fatigue tensile failure tests were conducted on as-drawn wires subjected to defined current amplitudes and cycle counts. Test conditions included the following: 0.35 A for 100, 200, and 300 cycles (0.35-C100, C200, C300); 0.37 A for 20, 40, 100, 200, and 300 cycles (0.37-C20 to C300); and 0.39 A and 0.41 A for 20 and 40 cycles (0.39-C20/C40; 0.41-C20/C40). A current amplitude of 0.37 A was used as the threshold to distinguish between low- and high-current regions. Below this value, fracture behavior and degradation were gradual and non-catastrophic. In contrast, currents at or above 0.37 A consistently induced rapid oxide thickening, interfacial cracking, and brittle fracture within a limited number of cycles. Accordingly, the results are discussed in two sections based on this transition in failure mode.

# 2.4. Fracture and Microstructure Characterization

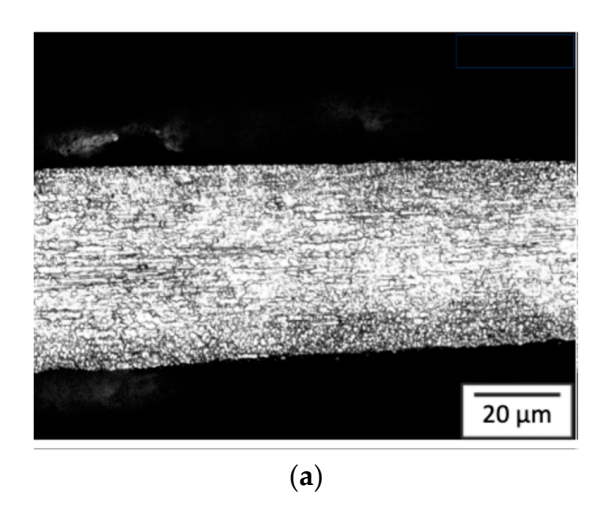
Fracture characterization included scanning electron microscopy (SEM, SU-5000, Hitachi, Tokyo, Japan) with energy-dispersive X-ray spectroscopy (EDS) and field-emission electron probe microanalysis (EPMA, JXA-8900R, JEOL, Tokyo, Japan) to examine fracture morphology, crack propagation, and the evolution of oxide layers. X-ray diffraction (XRD, D8 Discover, Bruker, Billerica, MA, USA) was performed over a  $2\theta$  range of 30–90° to analyze phase transformations before and after electrical fatigue. Optical microscopy (BX41M-LED, Olympus, Tokyo, Japan) was used for microstructural examination, and samples were chemically etched with an HNO<sub>3</sub>:HCl:  $H_2O = 1.3.4$  solution to reveal microstructure.

Collectively, the experimental procedures, including electrical fatigue cycling, current-assisted tensile testing, and post-fracture microstructural analyses, were designed to replicate service-relevant electrothermomechanical conditions encountered by fine-wire probe springs. This integrative approach enables correlation between applied electrical loading, microstructural evolution, and performance degradation, thereby forming the basis for the subsequent analysis and discussion.

#### 3. Results

#### 3.1. Microstructure of the Wire and Failure Resistance Under Different Tensile Strain Rates

Figure 4 displays the microstructure and microhardness (HV 508) of as-drawn 50 µm 631 SS wire, which may be attributed to the combined effects of severe cold drawing and strain-induced martensitic transformation [22]. A distinct radial grain size gradient is observed: the surface features fine grains formed by intense shear deformation during drawing, while the wire core retains larger, elongated grains aligned with the drawing direction. This elongated grain morphology indicates pronounced deformation-induced crystallographic texture [23], resulting in a microstructure characterized by both grain refinement and strong texture.



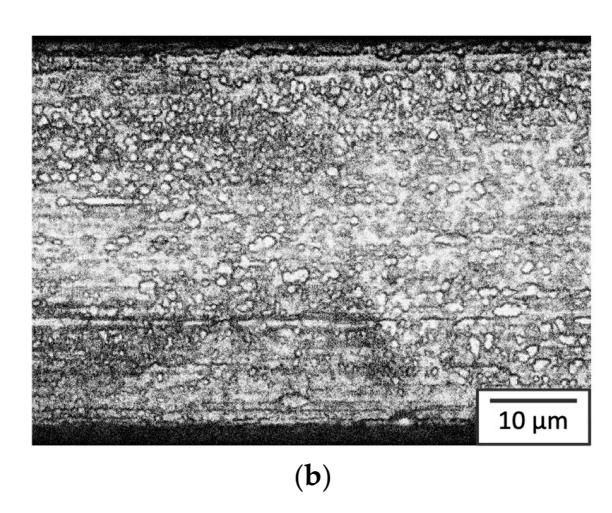


**Figure 4.** Microstructure of 50  $\mu$ m 631SS fine wire: (a)  $50\times$ ; (b)  $100\times$  image.

Uniaxial tensile tests were performed at engineering strain rates ranging from  $5.0 \times 10^{-3}$  to  $2.0 \times 10^{-2}$  s<sup>-1</sup> (corresponding to crosshead speeds of 15, 30, 45, and 60 mm/min). These strain rates were specifically selected to simulate the cyclic compression–release conditions encountered by probe springs in service, enabling evaluation of the wire's strain-rate sensitivity under application-relevant loading. As shown in Figure 5, the 50 µm-diameter wire achieves an ultimate tensile strength (UTS) exceeding 3000 MPa, a notably high value even for martensitic stainless steels, primarily attributable to combined martensitic transformation strengthening, strong texture, and severe work hardening [24]. Both UTS and yield strength (YS) remain essentially unchanged across the investigated strain rates, indicating negligible strain-rate sensitivity in terms of strength. In contrast, total elongation (TE) decreases with increasing strain rate, reflecting reduced ductility at higher deformation speeds.

Appl. Sci. 2025, 15, 8572 7 of 24

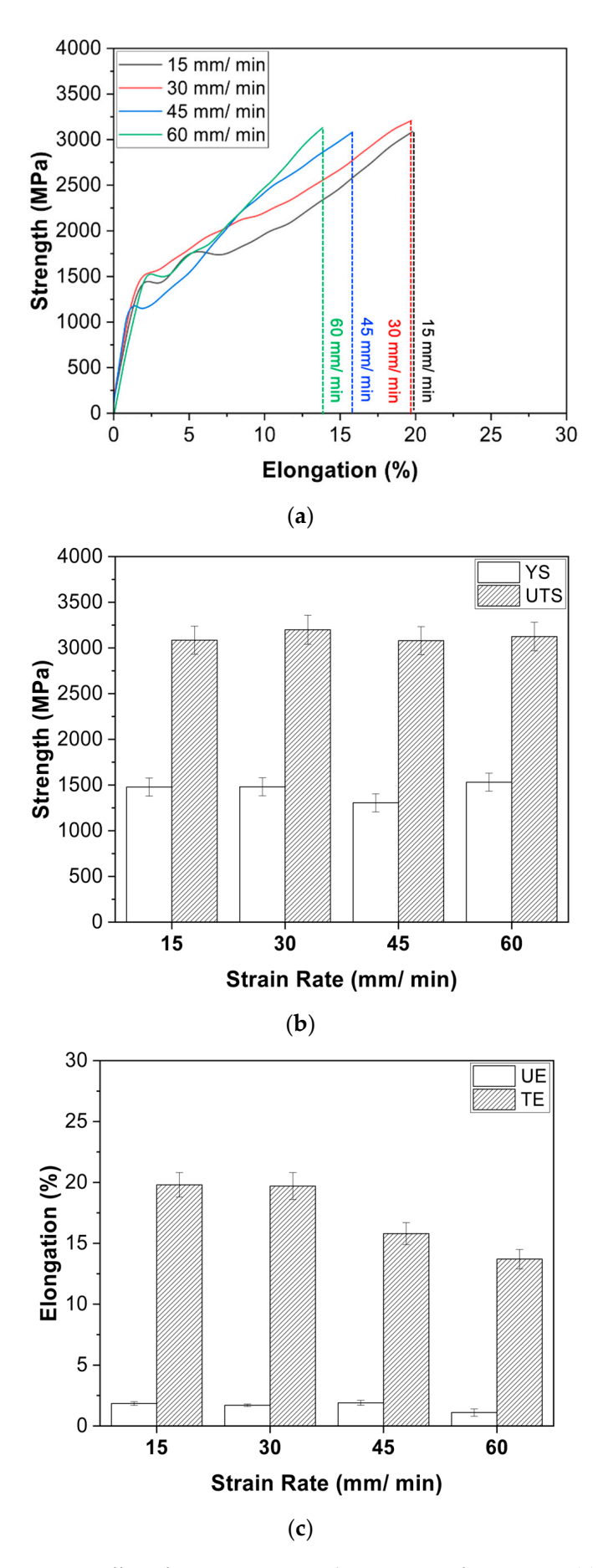


**Figure 5.** Effect of strain rate on tensile properties of 631SS wire: (a) Strength-elongation curve; (b) YS and UTS; (c) UE and TE.

# 3.2. Dynamic Electrical Characteristic Analysis of Wire After Quantitative Straining

To investigate strain-induced changes in electrical response at room temperature, we recorded I–V curves of 50  $\mu$ m 631 SS wires under controlled uniaxial tension as a practical proxy for the compressive cycles of probe springs, acknowledging that tensile and compressive elastic energies are equivalent only within the elastic regime ( $\epsilon \leq 0.5\%$ ). However, to capture the full range of service-relevant deformation, we extended these tests into plastic regions ( $\epsilon = 1.5\%$ , 5.0%, 10%, and 15%).

Strain levels were selected to span the elastic ( $\epsilon$  = 0.5%), yield ( $\epsilon$  = 1.5%), early plastic ( $\epsilon$  = 5.0%), moderate plastic ( $\epsilon$  = 10%), and near-ultimate tensile strength (UTS) ( $\epsilon$  = 15%) regions. Measurements I–V (Figure 6a,b) show negligible differences at the low current region (<0.3 A) but a monotonic increase in resistance at the higher current region (>0.3 A). I<sub>fuse</sub> after strain remains almost the same (Table 2).

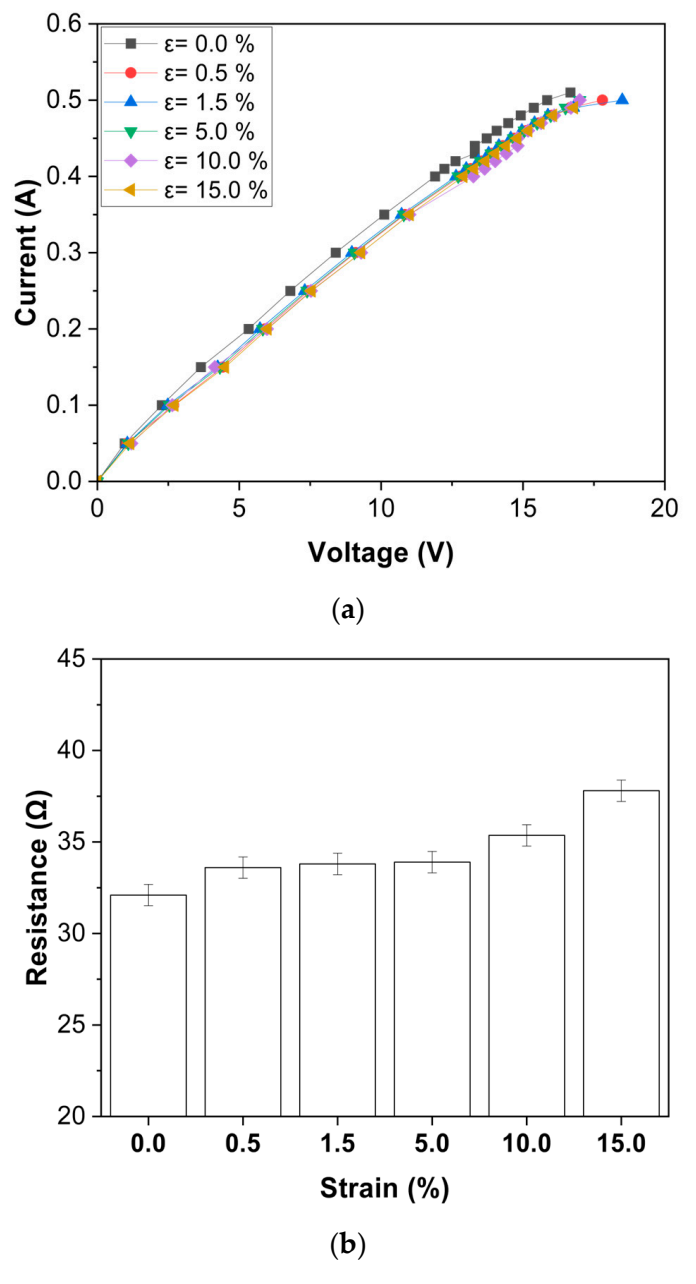


**Figure 6.** Electrical properties: (a) I–V characteristics; (b) resistance of 631SS wire after quantitative tensile strain.

Appl. Sci. 2025, 15, 8572 9 of 24

**Table 2.** I<sub>fuse</sub> of 631 wire quantitative tensile strain.

Strain (%)	0	0.5	1.5	5	10	15
FC (A)	0.51	0.5	0.5	0.5	0.5	0.49

# 3.3. Wire Electrical Fatigue Lifespan

Electrical fatigue was evaluated by cycling fine 50  $\mu$ m 631 SS wires at fractions of their I<sub>fuse</sub> (0.52 A), corresponding to current densities between 1.53  $\times$  10<sup>4</sup> and 2.09  $\times$  10<sup>4</sup> A/cm², as listed in Table 1. The fatigue-life versus current relationship (Figure 7a) divides naturally into three regions: (1) rapid failure (<10 cycles) at 90–85% I<sub>fuse</sub>; (2) intermediate life (50–100 cycles) at 80–75% I<sub>fuse</sub>; and (3) long life (>15,000 cycles) below 58% I<sub>fuse</sub>. This strong current dependence can be rationalized in terms of electron flux. An increase from 0.30 A (58% I<sub>fuse</sub>) to 0.47 A (90% I<sub>fuse</sub>) raises the electron flux by ~30%, intensifying Joule heating and electromigration, which accelerate oxide formation, defect accumulation, and crack initiation. Conversely, at  $\leq$ 0.35 A (<58% I<sub>fuse</sub>), Joule heating is comparatively moderate, oxidation is suppressed, and fatigue life is markedly prolonged. Figure 7b,c shows pronounced red luminescence and surface morphologies after fatigue, exhibiting current-dependent features.

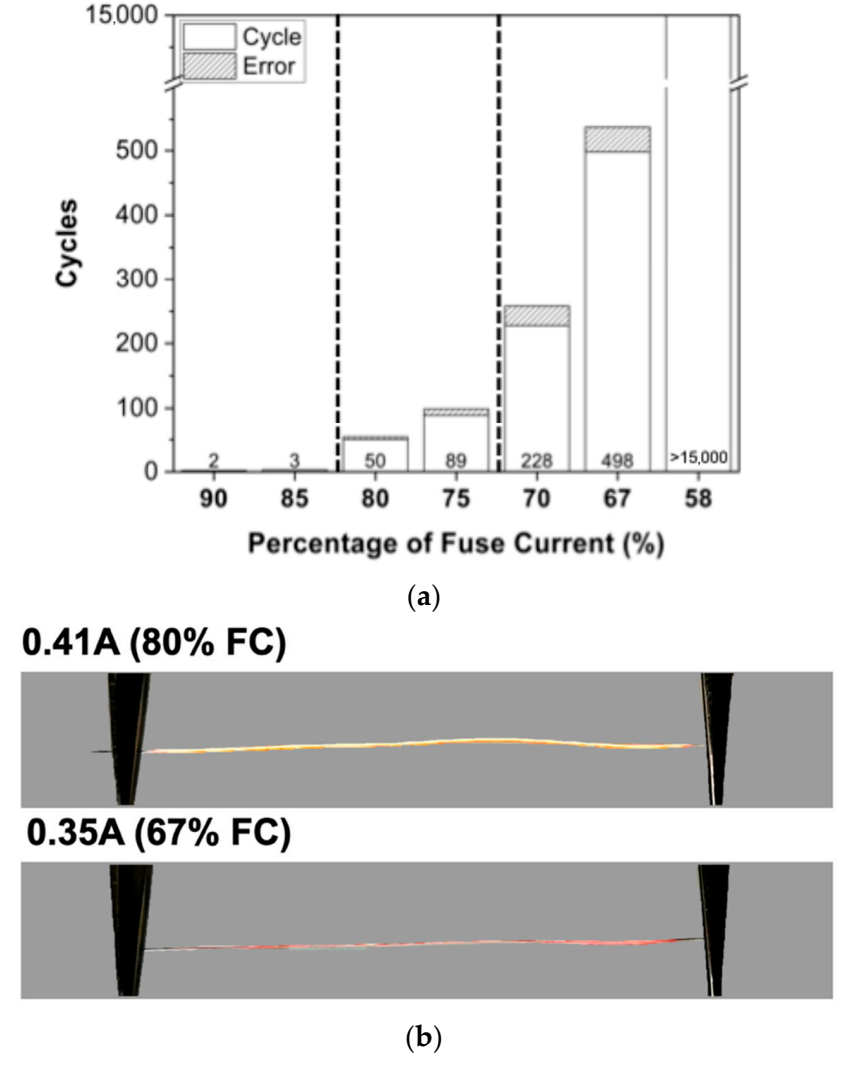
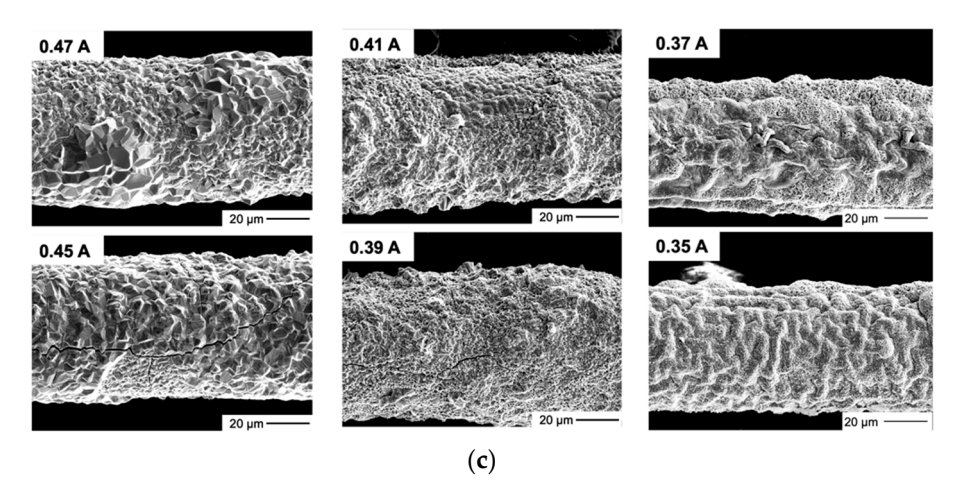


Figure 7. Cont.



**Figure 7.** Electrical fatigue properties: (a) Electrical fatigue life; (b) physical appearance; (c) surface morphology after fusing under different currents.

#### 3.4. Low-Current Electrical Fatigue: Electrical Properties and Wire Microstructure

Under low-current electrical-fatigue conditions (0.35 A and 0.37 A), electrical properties and microstructure were monitored up to 300 cycles. Beyond this point, severe embrittlement (0.35 A) and thermal fusing (0.37 A) prevented further testing; therefore, 300 cycles mark the beginning of irreversible degradation.

Resistance measurements (Figure 8) began at 100 cycles, once contact instability subsided and microstructural evolution became detectable. At this point, the two currents gave comparable resistance, providing a common baseline. Beyond 100 cycles, resistance decreased at 0.35 A but increased at 0.37 A, indicating competing recovery and oxidation-driven mechanisms. XRD, optical microscopy, and EPMA analyses of the 0.35-C200 and 0.37-C200 specimens (Figures 9–11) were performed to investigate this divergence. (Figures 9–11).

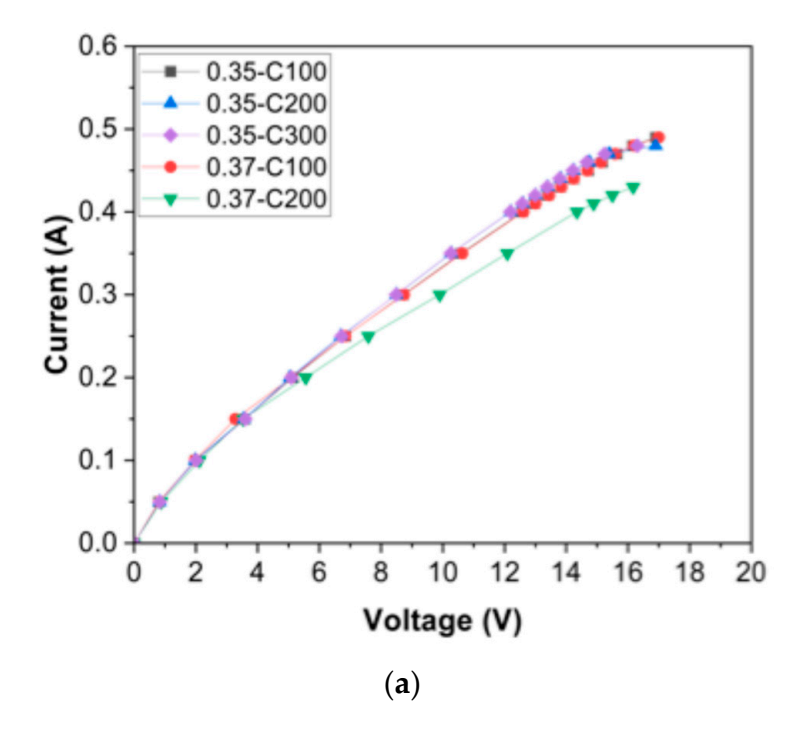
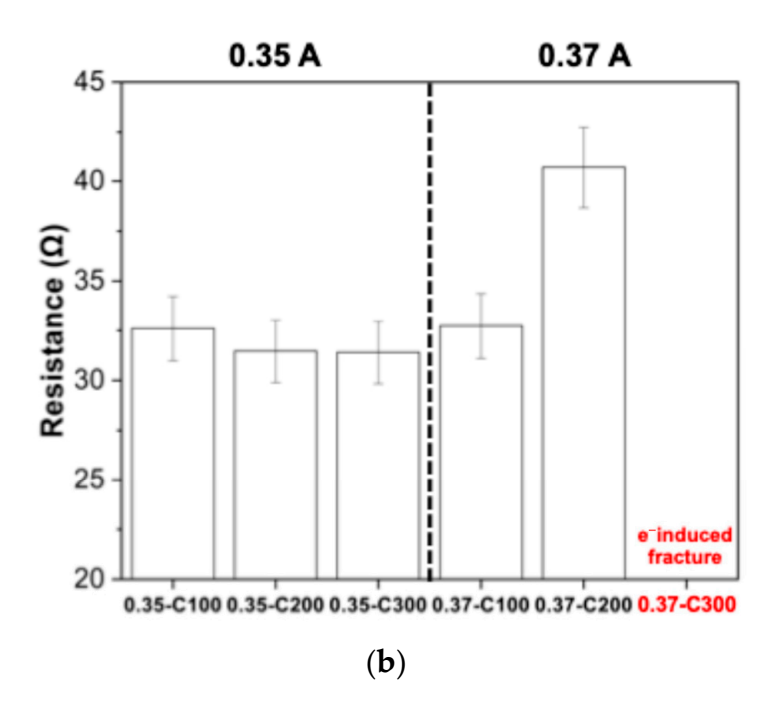


Figure 8. Cont.



**Figure 8.** Electrical properties: (a) I–V characteristics; (b) resistance behavior after high-cycle electrical fatigue at 0.35 A and 0.37 A.

The as-received wire consisted predominantly of strain-induced martensite with high dislocation density. XRD, optical microscopy, and EPMA (Figures 9–11) of 0.35-C200 revealed a uniform ~1.4  $\mu$ m Cr<sub>2</sub>O<sub>3</sub>/SiO<sub>2</sub>/Al<sub>2</sub>O<sub>3</sub> oxide layer and an approximately 5% narrowing of the (110) peak FWHM, indicating partial lattice-strain relaxation and homogeneous grain growth [25]. In contrast, the 0.37-C200 specimen developed a thicker ~3.8  $\mu$ m scale dominated by Fe<sub>2</sub>O<sub>3</sub>, Cr<sub>2</sub>O<sub>3</sub>, SiO<sub>2</sub>, and Al<sub>2</sub>O<sub>3</sub>—reducing the conductive cross-section by approximately 15% and sharply increasing resistance. Subsurface EPMA mapping identified fine carbides and Al–Si-rich phases.

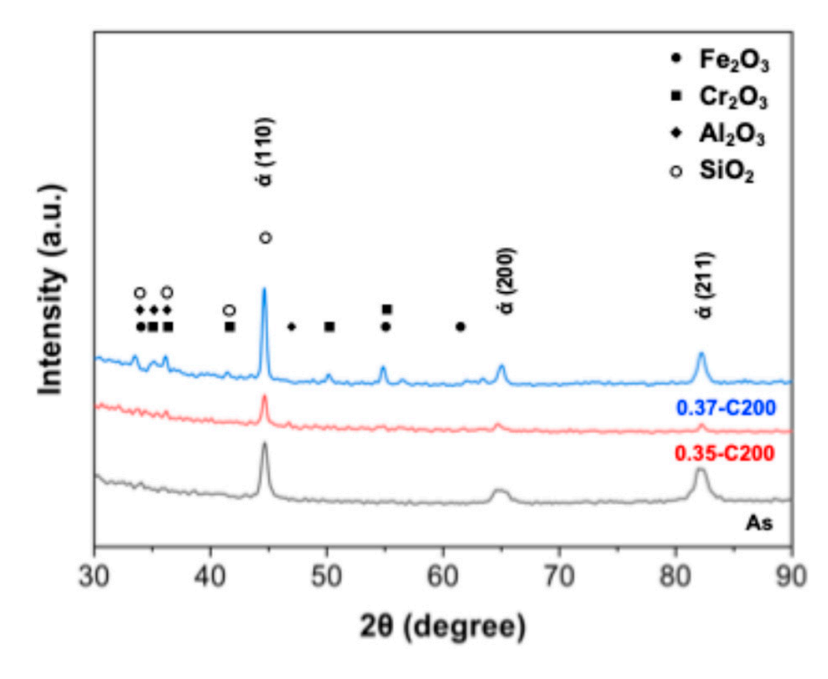


Figure 9. X-Ray diffraction pattern of As, 0.35-C200 and 0.37-C200.

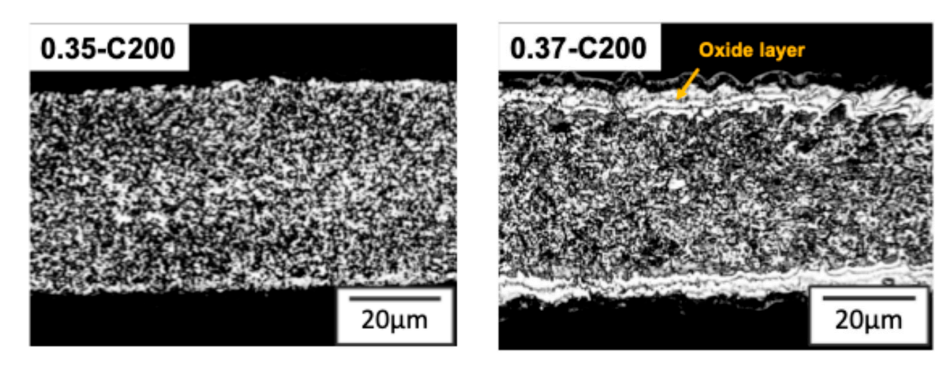
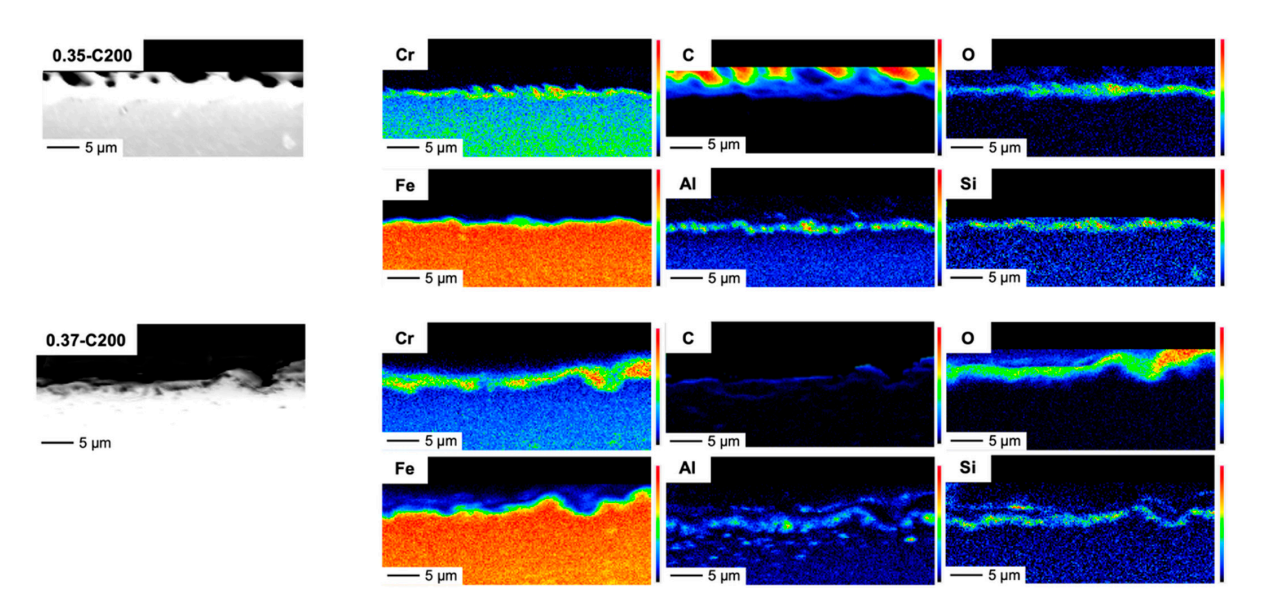


Figure 10. Microstructure and oxide layer thickness of 0.35-C200 and 0.37-C200.



**Figure 11.** EPMA mapping shows a  $\sim$ 1.4 µm oxide layer in 0.35-C200 and a thicker  $\sim$ 3.8 µm Fe-rich scale in 0.37-C200.

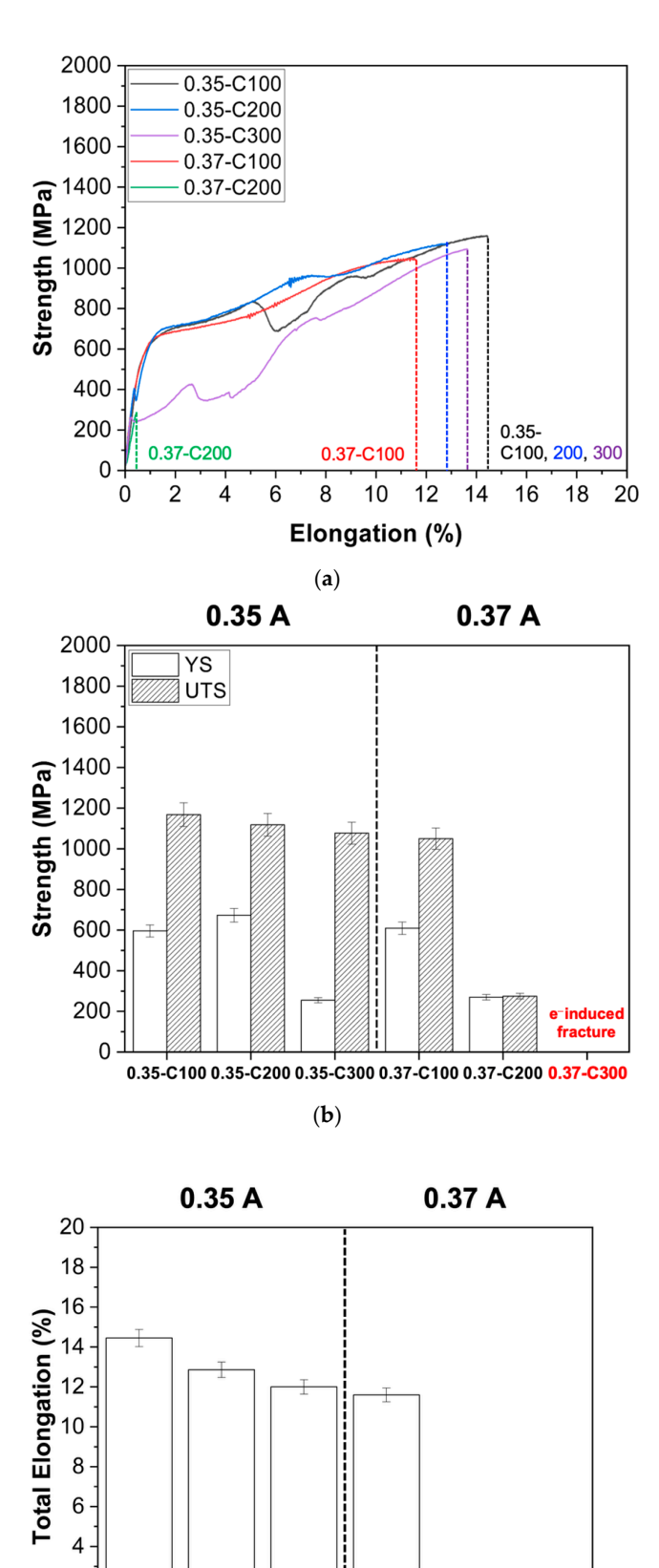
 $I_{\rm fuse}$  data (Table 3) support these trends: oxide growth at 0.37 A significantly reduces  $I_{\rm fuse}$ , leading to accelerated thermal failure, whereas 0.35 A maintains a stable  $I_{\rm fuse}$  with recovery-enhanced conductivity. Overall, 0.35 A favors uniform recovery and stability, while 0.37 A causes oxidation-dominated degradation.

**Table 3.** I<sub>fuse</sub> after high-cycle electrical fatigue at 0.35 A and 0.37 A.

Sample	0.35-C100	0.35-C200	0.35-C300	0.37-C100	0.37-C200	0.37-C300
FC (A)	0.49	0.48	0.48	0.49	0.43	X

#### 3.5. Tensile Fracture Mechanism Under Low-Current Electrical Fatigue

Tensile tests on wires fatigued at 0.35 A and 0.37 A (Figure 12) were conducted to quantify the effects of cyclic electrothermal loading on mechanical strength. For the 0.35 A condition, the UTS remains nearly constant after 100, 200, and 300 cycles, indicating that extended low-current cycling does not further impair tensile performance. Relative to the as-received state, the UTS at 0.35 A decreased by  $\sim$ 50%, reflecting a partial loss of coldwork strengthening due to Joule-heating-driven dislocation recovery. This microstructural softening, discussed in Section 4.3, is not accompanied by a significant loss of ductility. SEM images of the fracture surfaces (Figure 13a,b) reveal uniformly deformed profiles with no signs of interfacial decohesion or early cracking on the  $Cr_2O_3$ -rich surface oxide layer (Figure 14a).



0.35-C100 0.35-C200 0.35-C300 0.37-C100 0.37-C200 0.37-C300 (c)

0

**Figure 12.** Tensile properties of 631SS wire: (a) Strength-elongation curve; (b) YS and UTS; (c) TE after 0.35 and 0.37 A electrical fatigue.

e-induced

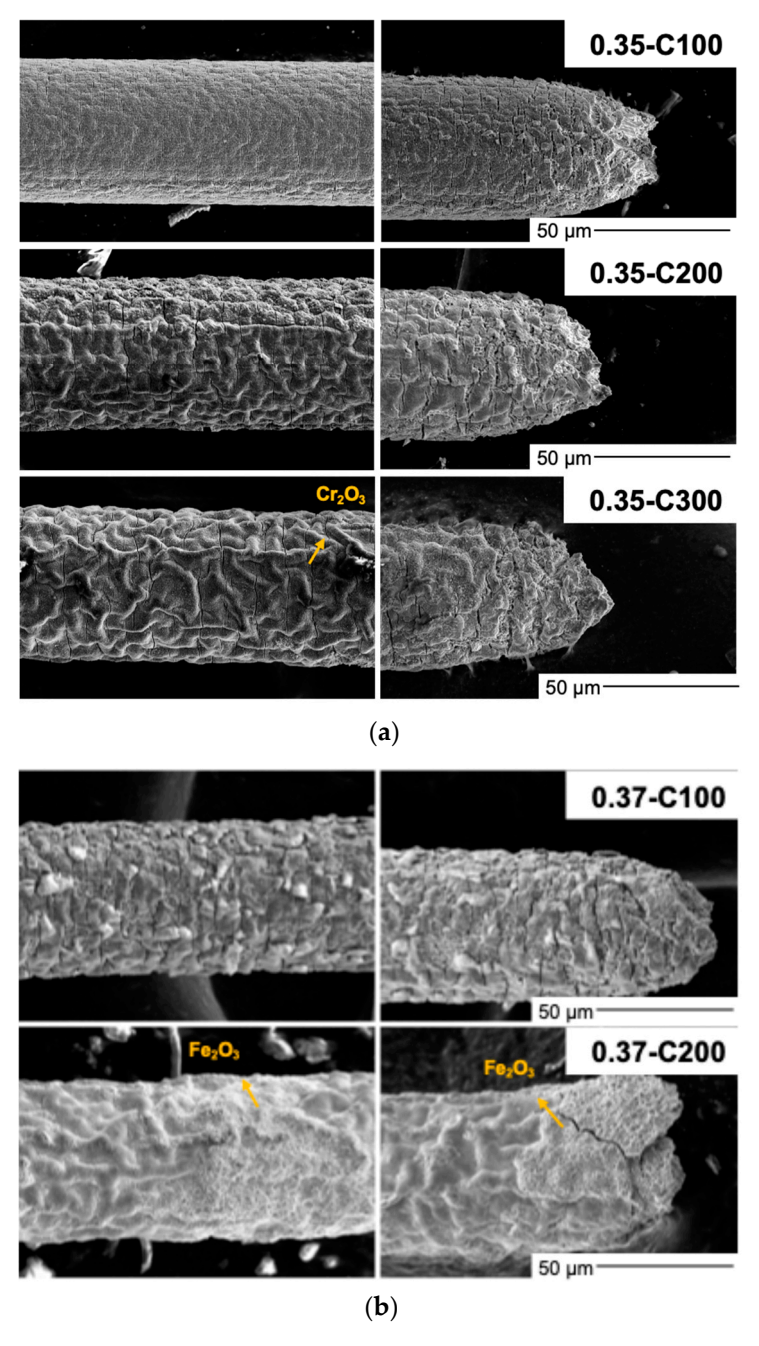


Figure 13. Surface and fracture morphology after electrical fatigue: (a) At 0.35 A; (b) At 0.37 A.

The  $Cr_2O_3$ -rich surface oxide layer indicates mechanical compatibility with the underlying matrix. This behavior supports the interpretation that oxidation remains superficial and does not compromise fracture integrity at this current level [26,27].

In contrast, 0.37 A cycling leads to continuous declines in UTS, YS, and TE as the cycle count increases (Figure 12). Distinct changes in fracture morphology accompany the decline in ultimate tensile strength (UTS), yield strength (YS), and total elongation (TE). SEM fracture images (Figure 13b) reveal increasing crack density near the surface, which correlates with the growth of a  $Fe_2O_3$ -containing oxide layer and localized grain coarsening. Surface cracks frequently originate at the oxide–matrix interface and propagate inward, fragmenting the ductile zone. EDS mapping (Figure 14b) further confirms the presence of  $Fe_2O_3$  within surface oxide regions and reveals that crack propagation is spatially correlated with Fe-rich domains.

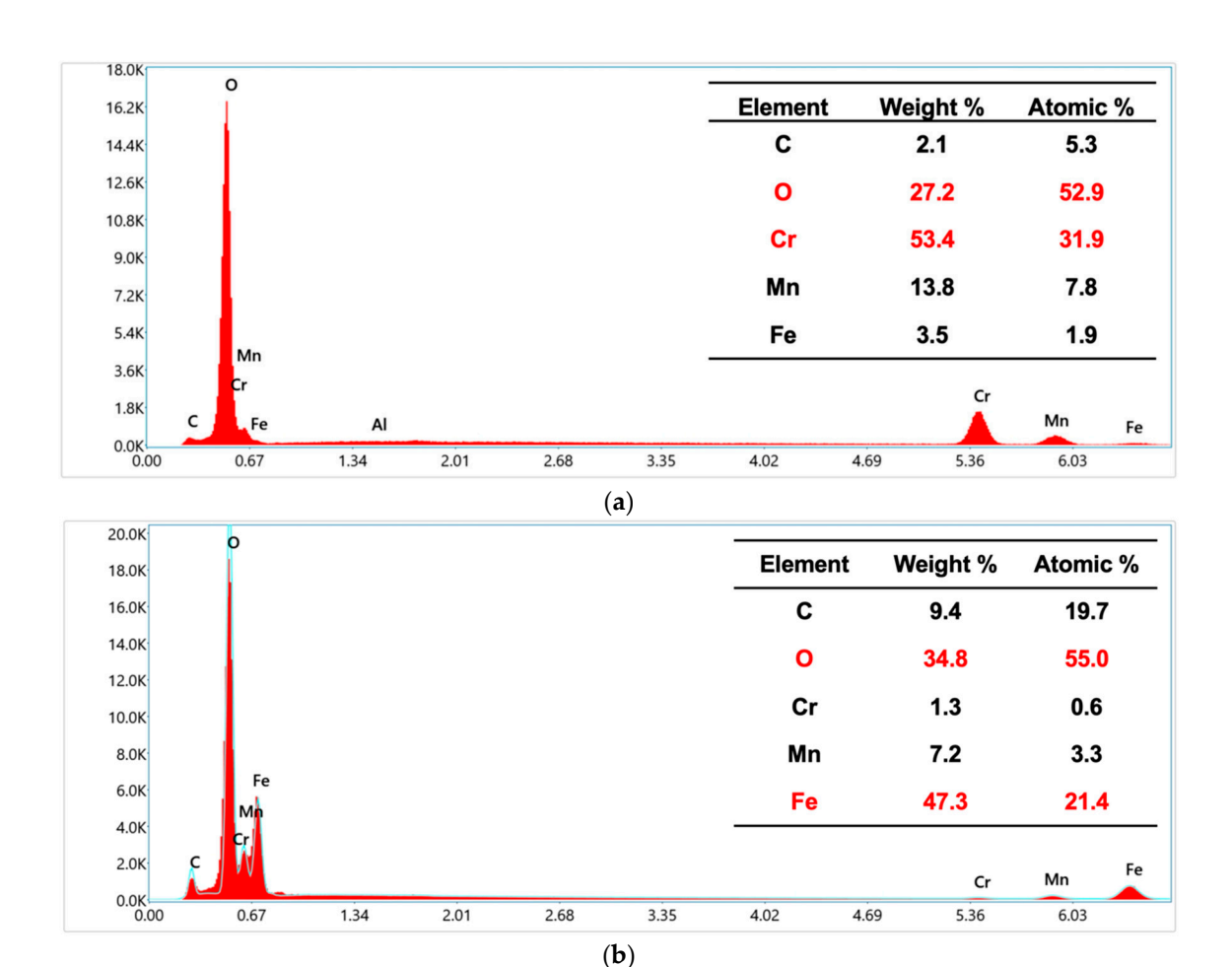


Figure 14. Surface element analysis after electrical fatigue: (a) 0.35-C200; (b) 0.37-C200.

3.6. High-Current Electrical Fatigue: Evolution of Electrical Properties and Wire Microstructure

Electrical-fatigue tests were extended to 0.37, 0.39, and 0.41 A. Since the 0.41 A specimens failed in fewer than 50 cycles, microstructural analyses focused on the 20- and 40-cycle. In the low-current regime (<0.30 A), the I–V curves (Figure 15) show identical conductance, confirming negligible resistance change. Above 0.30 A, the responses diverge: resistance falls slightly at 0.37 A, rises modestly at 0.39 A, and climbs sharply at 0.41 A. I $_{\text{fuse}}$  values (Table 4) follow the same order and drop steeply as 0.41 A approaches failure.

Table 4.  $I_{fuse}$  after low-cycle 0.37 A, 0.39 A and 0.41 A electrical fatigue.

Sample	0.37-C20	0.37-C40	0.39-C20	0.39-C40	0.41-C20	0.41-C40
FC (A)	0.5	0.49	0.49	0.49	0.48	Χ

XRD from 40-cycle specimens (Figure 16) exhibit a dual-phase martensite ( $\alpha'$ ) and austenite ( $\gamma$ ) matrix with oxide (Al<sub>2</sub>O<sub>3</sub>, SiO<sub>2</sub>, Cr<sub>2</sub>O<sub>3</sub>).  $\gamma$  peaks are attributed to metastable, carbon-enriched austenite formed by early-stage outward carbon diffusion; these peaks disappear with extended cycling as the phase decomposes and forms fine carbides [28,29]. SEM imaging (Figure 17) reveals oxide layers in both 0.37-C40 and 0.39-C40 specimens, with increased void density and surface roughness at the higher current. EPMA mapping (Figure 18) confirms Cr<sub>2</sub>O<sub>3</sub>-dominated scales with localized Al-Si enrichment and carbon segregation, indicative of interdiffusion and thermally activated carbon migration [30].

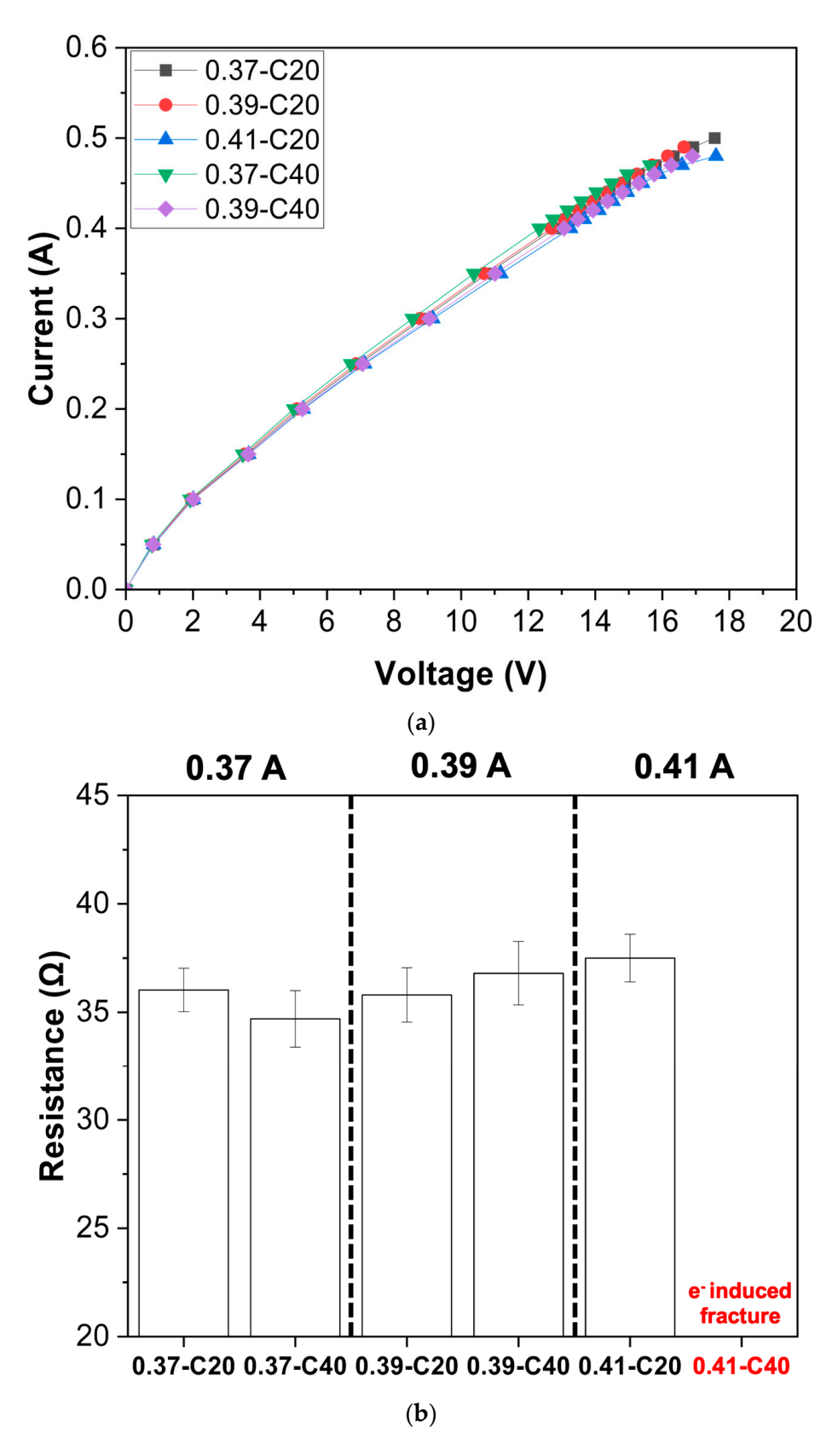


**Figure 15.** Electrical properties: (**a**) I–V characteristics; (**b**) resistance behavior after electrical fatigue at 0.37 A, 0.39 A, and 0.41 A.

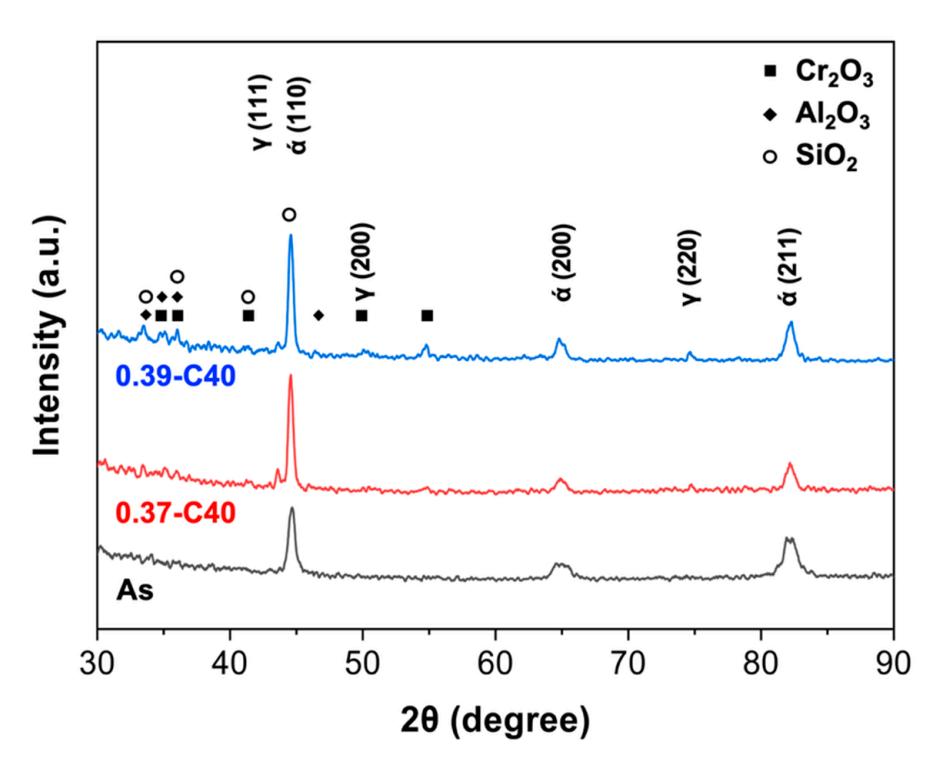


Figure 16. X-ray diffraction pattern of As, 0.37-C40, and 0.39-C40.

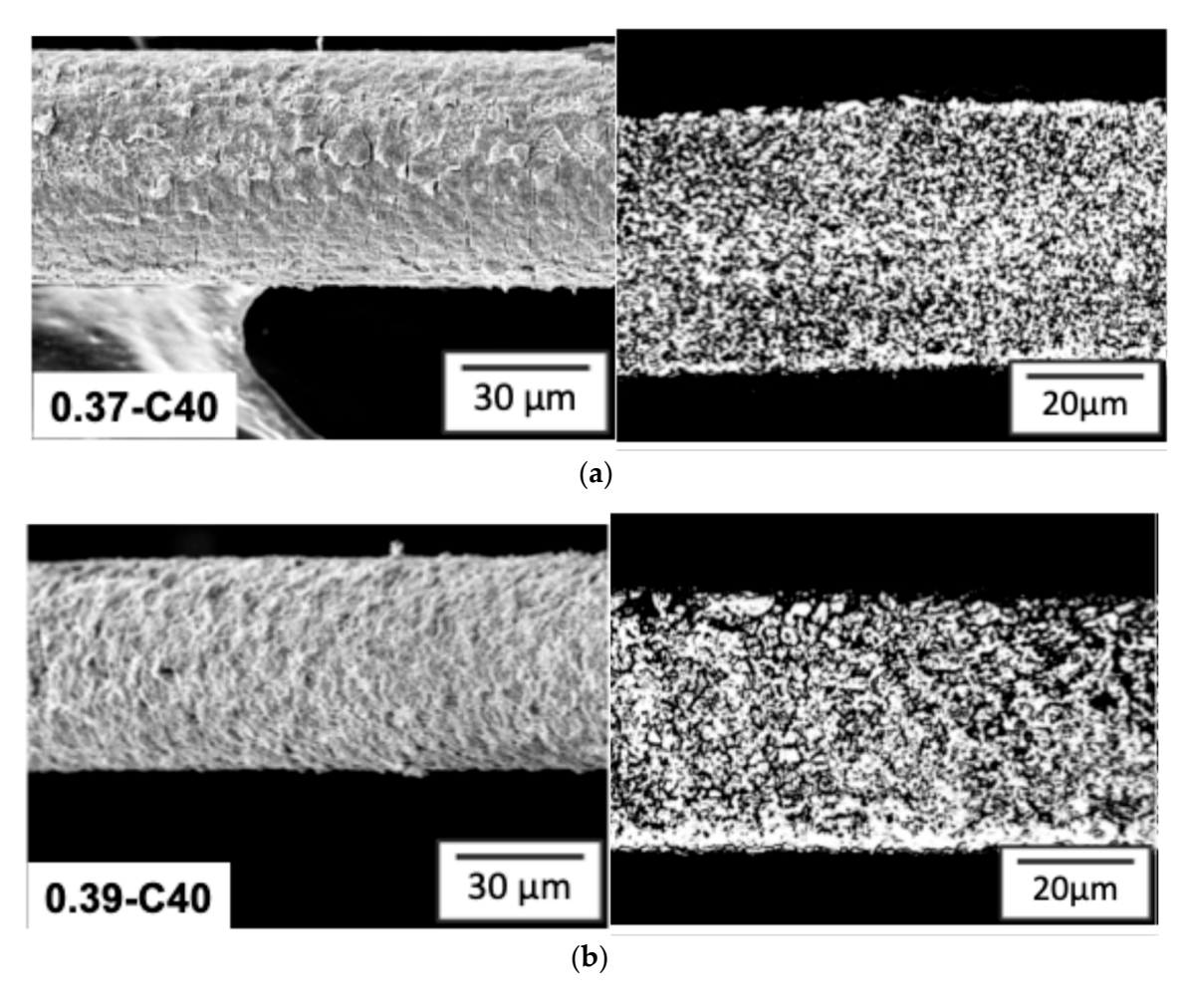
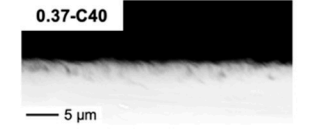
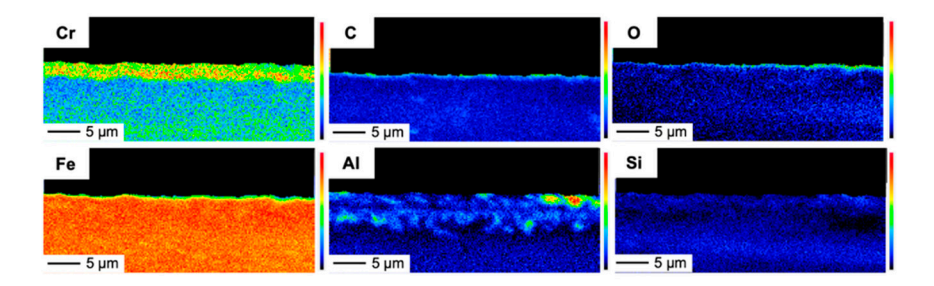


Figure 17. Surface morphology and microstructure: (a) 0.37-C40; (b) 0.39-C40.

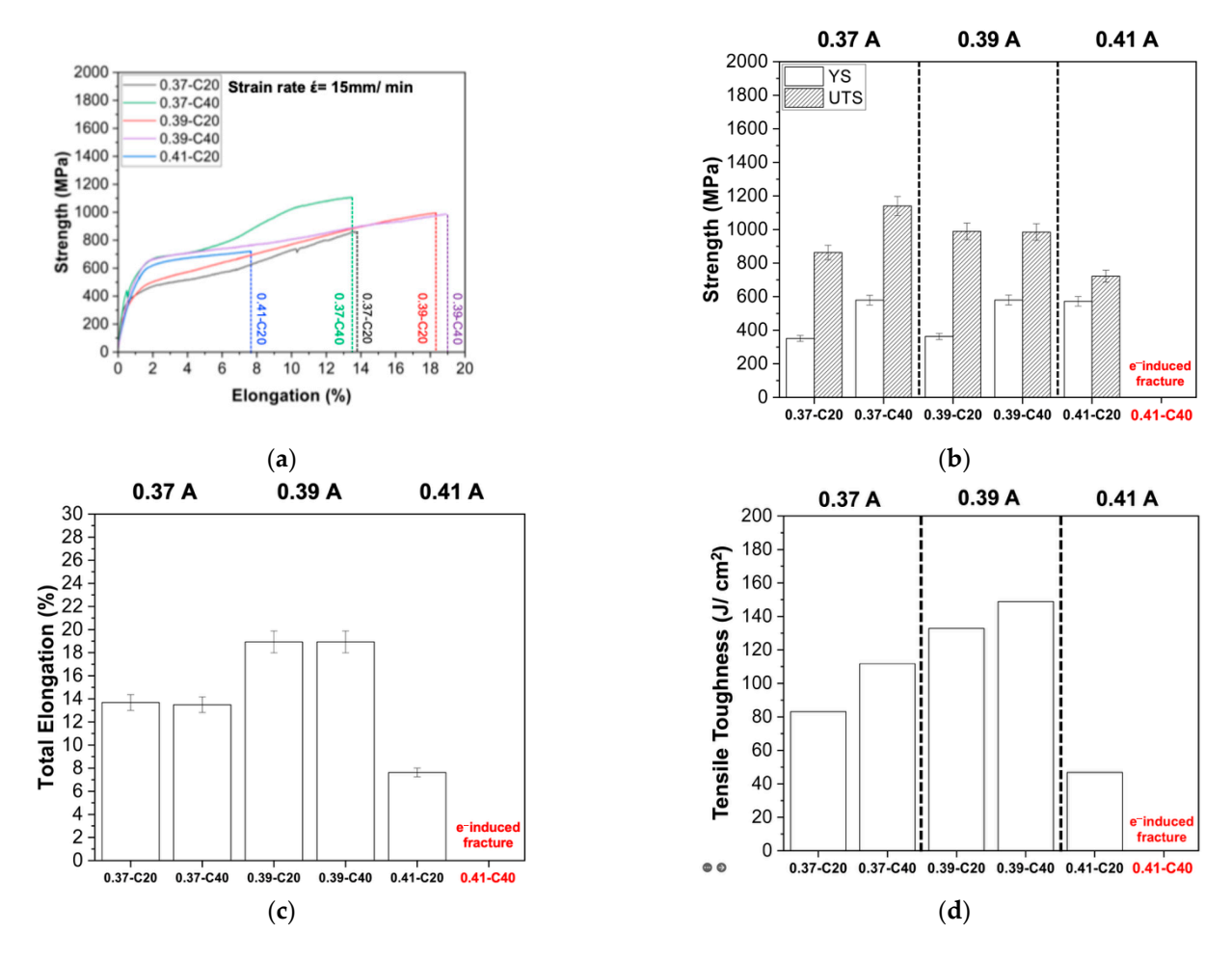




**Figure 18.** EPMA elemental mapping of the 0.37-C40 sample after cyclic electrothermal loading: Cr<sub>2</sub>O<sub>3</sub>-rich oxide, with Al-Si enrichment and subsurface carbon segregation.

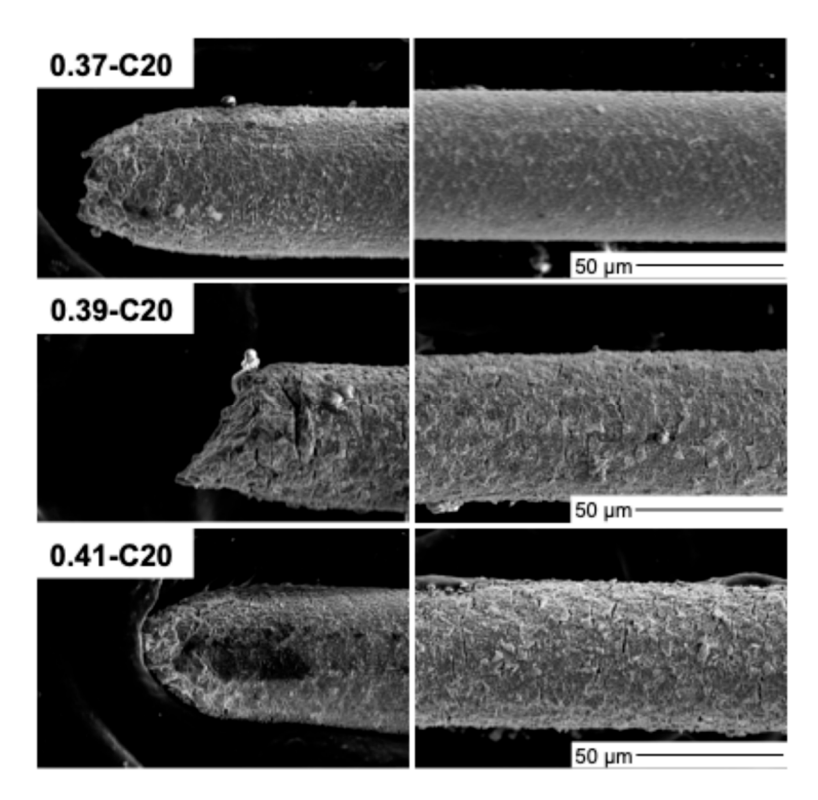
#### 3.7. Tensile Fracture Mechanism Under High-Current Electrical Fatigue

Post-electrical fatigue tensile testing (Figure 19) reveals that 0.39 A cycling enhances total elongation and toughness [31] despite minor reductions (~10%) in YS and UTS relative to 0.37 A. This response is attributed to the temporary presence of carbon-stabilized  $\gamma$ -austenite (Figure 16), which, together with moderate recovery, enhances the ductility [32].



**Figure 19.** Tensile properties of 631SS wire: (a) Strength-elongation curve; (b) YS and UTS; (c) TE; and (d) tensile toughness after low-cycle 0.37 A, 0.39 A, and 0.41 A electrical fatigue.

In contrast, 0.41 A specimens show concurrent declines in strength, elongation, and toughness, indicative of early embrittlement. SEM fracture analysis (Figure 20) reveals ductile failure in the 0.39-C20 specimen.



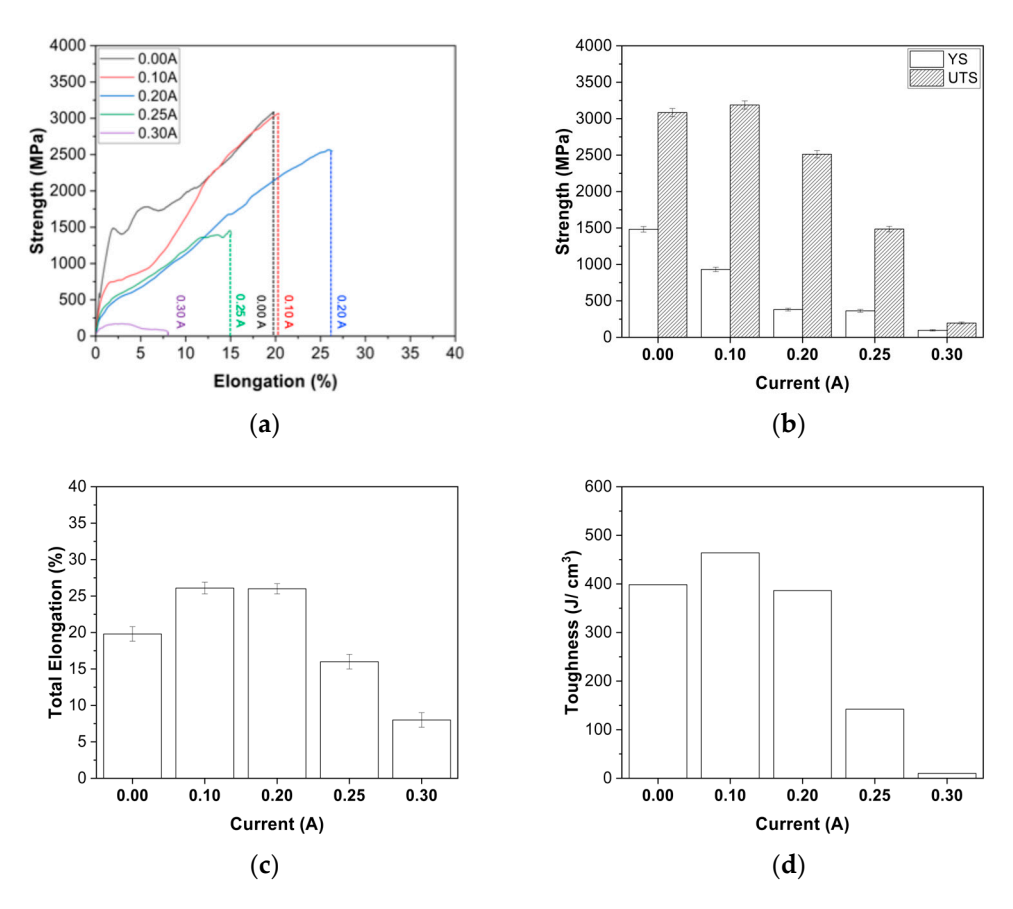
**Figure 20.** Surface morphology and tensile fracture surface after electrical fatigue: 0.37-C20, 0.39-C20, and 0.41-C20.

Figure 19 summarizes the tensile properties and toughness obtained from the integrated area under the engineering stress-strain curve of 631 stainless-steel wire after high-current electrical fatigue. Relative to 0.37 A, cycling at 0.39 A raises the total elongation (TE) and increases tensile toughness, albeit at the expense of a  $\approx$ 10% drop in yield strength (YS) and ultimate tensile strength (UTS). In sharp contrast, the 0.41 A condition exhibits concurrent reductions in strength and ductility, resulting in a lower tensile toughness compared to the 0.37 A group. XRD analysis (Figure 16) reveals a transient, carbon-stabilized austenitic ( $\gamma$ ) peak after 0.39 A cycling but not after 0.41 A. The  $\gamma$  phase, in conjunction with moderate electrothermal recovery, may delay strain localization and thereby enhance tensile toughness [33].

#### 3.8. Current-Assisted Tensile Testing and Thermal Simulation Conditions

The result of the current-assisted tensile test is shown in Figure 21. At 0.10 A ( $\approx$ 63 °C), the wire shows a modest rise in total elongation (TE), while the ultimate tensile strength (UTS) remains essentially unchanged relative to the cold-drawn baseline. Although 63 °C is far below the recrystallization temperature for 631 stainless steel, the cold-drawn wire retains a high dislocation density and stored energy due to the severe drawing. A small thermal increment enables slight dislocation rearrangement and dynamic recovery during the short (<30 s) tensile-loading window [21]. Increasing the current to 0.20 A ( $\approx$ 202 °C) produces a modest ( $\sim$ 5%) reduction in ultimate tensile strength (UTS), whereas total elongation (TE) is higher than at the 0.10 A level.

Elevating the current to 0.25 A raises the wire temperature to  $\approx 308$  °C. At this temperature, recovery occurs, sharply reducing dislocation density and work-hardening. As a result, both YS and UTS dropped by roughly 50%. Concurrently, oxide growth produces surface grooves and microvoids that trigger early necking; the total elongation (TE) falls by a comparable amount. At 0.30 A (445 °C), the wire fails in a brittle manner during electrically assisted tension because the temperature falls within the thermal-softening region.



**Figure 21.** 631SS wire current-assisted tensile test under different current: (a) Strength-elongation curve; (b) YS and UTS; (c) TE; and (d) tensile toughness.

#### 4. Discussion

#### 4.1. Electrical Change Following Quantitative Straining

The resistance rise originates from lattice distortion and area reduction at  $\varepsilon$  < 5% and from dislocations and defects at  $\varepsilon$  > 10% [34]. Crucially, within the elastic-to-early-plastic window ( $\varepsilon$   $\leq$  5%), resistance variation remains minimal, confirming that moderate deformation, even beyond the purely elastic limit, does not compromise electrical stability or fuse current.

# 4.2. Electrical Fatigue Failure Mechanisms of Wire

Visual evidence (Figure 7b,c) confirms pronounced red luminescence and surface morphologies after fatigue exhibit current-dependent features: (1) at extremely high current levels (0.47–0.45 A), ridge-like oxide structures form due to localized melting and rapid oxidation; (2) at high currents (0.41–0.39 A), granular oxide layers dominate; and (3) at low currents ( $\leq$ 0.37 A), the surface retains fine metal flow lines with oxidation. The narrow 0.35–0.41 A window thus marks the transition from comparably thermally stable operation to oxidation-driven degradation and should be the focus of targeted fatigue-failure studies.

# 4.3. Electrical Characteristic, Microstructure Evolution, and Tensile Fracture Mechanism After Low-Current Electrical Fatigue

Under 0.35 A cycling, the electrothermal input is sufficient to activate uniform dynamic recovery and grain coarsening, leading to partial softening, while oxidation remains limited and non-detrimental. The dominant mechanism at the 0.35 A condition is therefore interpreted as a benign annealing effect, which stabilizes both mechanical and electrical properties without inducing critical surface degradation. In contrast, the 0.37-C200 subsur-

face EPMA mapping identified fine carbides and Al–Si-rich phases, indicative of localized overheating [26]. Subsurface carbide concentration further suggests thermally driven carbon migration consistent with electrothermal diffusion [35]. Although the (110) peak's FWHM narrows by about 10 %, compared to 5 % for 0.35-C200, the dominant contribution to resistance increase is the thick, insulating Fe<sub>2</sub>O<sub>3</sub>-rich oxide scale (~3.8  $\mu$ m). Optical microscopy further reveals heterogeneous grain coarsening, indicating non-uniform Joule heating that enhances, but does not exceed, the impact of surface oxidation on electrical degradation.

The  $Cr_2O_3$ -rich surface oxide layer on the 0.35A sample indicates mechanical compatibility with the underlying matrix. This behavior supports the interpretation that oxidation remains superficial and does not compromise fracture integrity at this current level. The observation of 0.37A sample is consistent with the intrinsic brittleness of  $Fe_2O_3$  and its tendency to act as a crack initiation site under tensile loading [36]. These findings support the conclusion that oxidation-induced surface embrittlement, rather than microstructural recovery, dominates the fracture evolution under elevated current fatigue.

# 4.4. Electrical Characteristic, Microstructure Evolution, and Tensile Fracture Mechanism After High-Current Electrical Fatigue

A modest increase in current from 0.37 A to 0.41 A shifts the predominant mechanism from recovery-driven stabilization to oxidation-facilitated degradation. At 0.37 A, uniform recovery surpasses early oxidation, resulting in a marginal decrease in resistance. Elevated currents induce non-uniform scale thickening and interfacial instability; at 0.41 A, an abrupt increase in resistivity and oxide-induced damage indicates the initiation of surface-driven failure under heightened Joule heating. Under 0.37A current loading, strain delocalization was observed, suggesting improved deformation uniformity and enhanced ductility. This behavior suggests that moderate Joule heating can promote dislocation mobility or partial recovery, thereby reducing strain localization. At 0.39 A, the wire response appears transitional; although ductility stayed favorable, signs of interfacial degradation appeared through localized surface oxidation. This intermediate regime likely represents a threshold where thermal softening begins to counteract mechanical strengthening. At 0.41 A, extensive radial cracking and oxide delamination were observed on the fracture surface, indicating surface-driven decohesion and loss of structural integrity. These results delineate a critical transition from ductility-enhancing mechanisms to irreversible electrothermal degradation, governed by the intensification of localized heating and oxidation-induced embrittlement under elevated current conditions.

#### 4.5. Current-Assisted Tensile Testing Analysis

The 0.20A current-assisted tensile behavior reflects the onset of dislocation rearrangement and partial recovery of strain hardening. The thermal exposure at this level is adequate to facilitate local defect mobility but remains below the threshold for extensive grain coarsening or recrystallization [37]. Within the resolution of the present experiments, ductility is therefore enhanced while strength begins to decline. At 0.25A, the combined loss of strain-hardening ability and surface integrity explains the simultaneous decrease in strength and ductility, and even severe deterioration occurs at 0.30A.

For electrically conductive springs, operating currents should remain below 0.20 A to balance mild recovery-enhanced ductility against the onset of grain-growth-driven softening or oxide-related embrittlement.

Appl. Sci. 2025, 15, 8572 22 of 24

# 5. Conclusions

Following cold working, the as-drawn 631 stainless steel wire exhibits a predominantly martensitic microstructure with elongated grains and a very high dislocation density, resulting in a tensile strength exceeding 3 GPa. Under low-current electrical fatigue ( $\leq\!0.35$  A), electrothermal recovery relieves internal stress and stabilizes electrical resistance without compromising mechanical strength. In contrast, higher current cycling ( $\geq\!0.37$  A) promotes rapid Fe<sub>2</sub>O<sub>3</sub> scale growth and interfacial cracking, leading to strength degradation and premature fracture. These trends are further supported by electrically assisted tensile tests: a moderate current of 0.10 A ( $\approx\!63$  °C) slightly enhances elongation through partial recovery, whereas increasing the current to 0.25 A ( $\approx\!308$  °C) reduces work hardening and initiates oxidation-induced ductility loss. At 0.30 A ( $\approx\!445$  °C), severe grain coarsening and thermally activated surface damage cause brittle failure.

Taken together, the coupled cyclic electrothermal fatigue and electrically assisted tensile data establish a current- and temperature-bounded operating window for ultrahigh-strength 631 spring wire. Compared to previous studies on cold-drawn martensitic or precipitation-hardenable stainless wires tested under solely mechanical or thermal loads [36,38], this work offers a microstructure-based electrothermal failure map directly applicable to high current-density, probe-spring applications.

**Author Contributions:** Conceptualization, C.-T.H.; Methodology, C.-T.H.; Formal analysis, C.-T.H.; Investigation, C.-T.H.; Writing—original draft, C.-T.H.; Supervision, F.-Y.H. and K.-C.C. All authors have read and agreed to the published version of the manuscript.

Funding: This research received no external funding.

**Data Availability Statement:** The original contributions presented in this study are included in the article. Further inquiries can be directed to the corresponding author.

Acknowledgments: The authors would like to express their profound gratitude for the technical support and equipment generously provided by the Core Facility Center at National Cheng Kung University in Taiwan. Special acknowledgment is afforded to the Bruker D8D Plus-TXS and SU-5000 instruments for their invaluable assistance. Additionally, we wish to convey our sincere appreciation for the financial support received from the National Cheng Kung University Instrument Center and the Ministry of Science and Technology of Taiwan (NSTC 114-2221-E-006-126-MY3). Your contributions are greatly valued. They also thank Niche-Tech Group Limited for providing the wires and test equipment.

Conflicts of Interest: The authors declare no conflicts of interest.

#### References

- 1. Lee, D.; Cho, J.; Kim, C.H.; Lee, S.H. Application of laser spot cutting on spring contact probe for semiconductor package inspection. *Opt. Laser Technol.* **2017**, *97*, 90–96. [CrossRef]
- 2. Lee, M.K.; Lee, T.J.; Choi, H.W.; Shin, S.J.; Park, J.Y.; Lee, S.J. A Universal Spring-Probe System for Reliable Probing of Electrochemical Lab-on-a-Chip Devices. *Sensors* **2014**, *14*, 944–956. [CrossRef]
- 3. Wang, W.Y.; Liu, B.; Kodur, V. Effect of temperature on strength and elastic modulus of high-strength steel. *J. Mater. Civ. Eng.* **2013**, 25, 174–182. [CrossRef]
- 4. Lee, K.; Kim, B. MEMS spring probe for non-destructive wafer level chip test. *J. Micromechanics Microengineering* **2005**, *15*, 953. [CrossRef]
- 5. Hantschel, T.; Wong, L.; Chua, C.L.; Fork, D.K. Fabrication of highly conductive stressed-metal springs and their use as sliding-contact interconnects. *Microelectron. Eng.* **2003**, *67*, 690–695. [CrossRef]
- 6. Giordano, N. Experimental study of localization in thin wires. Phys. Rev. B 1980, 22, 5635. [CrossRef]
- 7. Glushko, O.; Cordill, M.J. In-operando fatigue behavior of gold metallization lines on polyimide substrate. *Scr. Mater.* **2020**, 186, 48–51. [CrossRef]
- 8. Zhang, H.; Sun, Q.; Sun, Z.; Lu, Y. Experimental and Numerical Investigation of Electromigration Behavior of Printed Silver Wire Under High Current Density. *J. Electron. Packag.* 2023, 145, 021006. [CrossRef]

9. Kimberley, J.; Chasiotis, I.; Lambros, J. Failure of microelectromechanical systems subjected to impulse loads. *Int. J. Solids Struct.* **2008**, 45, 497–512. [CrossRef]

- 10. Kolchuzhin, V.A.; Sheremet, E.; Bhattacharya, K.; Rodriguez, R.D.; Paul, S.D.; Mehner, J.; Hietschold, M.; Zahn, D.R. Mechanical properties and applications of custom-built gold AFM cantilevers. *Mechatronics* **2016**, *40*, 281–286. [CrossRef]
- 11. Lo, K.H.; Shek, C.H.; Lai, J.K.L. Recent developments in stainless steels. Mater. Sci. Eng. R Rep. 2009, 65, 39–104. [CrossRef]
- 12. Yang, J.L.; Li, Y.; Wang, F.; Zang, Z.G.; Li, S.J. New application of stainless steel. J. Iron Steel Res. Int. 2006, 13, 62–66. [CrossRef]
- 13. Moon, J.; Ha, H.Y.; Kim, K.W.; Park, S.J.; Lee, T.H.; Kim, S.D.; Lee, C.H. A new class of lightweight, stainless steels with ultra-high strength and large ductility. *Sci. Rep.* **2020**, *10*, 12140. [CrossRef] [PubMed]
- 14. Takahata, K.; Gianchandani, Y.B. Batch mode micro-electro-discharge machining. *J. Microelectromechanical Syst.* **2002**, *11*, 102–110. [CrossRef]
- 15. Tseng, C.Y.; Lin, J.W.; Tai, C.L.; Chung, T.F.; Yang, Y.L.; Tsao, T.C.; Lu, S.Y.; Chen, J.J.; Chiu, P.H.; Chen, C.Y.; et al. Effect of repeated-tempering induced martensite on the microstructural evolution in 17–7 PH stainless steel. *Mater. Charact.* 2024, 214, 114091. [CrossRef]
- 16. Peng, S.; Wei, Y.; Gao, H. Nanoscale precipitates as sustainable dislocation sources for enhanced ductility and high strength. *Proc. Natl. Acad. Sci. USA* **2020**, *117*, 5204–5209. [CrossRef]
- 17. Long, H.; Zhou, X.; Ma, Y.; Li, K.; Ren, J. The Effect of Heat Treatment on the Plasma Nitriding of Hot-Rolled 17–7 PH Stainless Steel. *Metals* **2024**, *14*, 1061. [CrossRef]
- 18. Yamasaki, S.; Takano, K. The Effect of Aging Conditions on the Stress Relaxation Behavior of 17-7PH Stainless Steel. In *Materials Science Forum*; Trans Tech Publications Ltd.: Bäch, Switzerland, 2021; Volume 1016, pp. 1664–1669.
- 19. Pervikov, A.V. Structural and phase transformations in zinc and brass wires under heating with high-density current pulse. *Phys. Plasmas* **2016**, 23. [CrossRef]
- Chang, Y.T.; Hung, F.Y.; Wu, B.D. Study on Material Properties and Copper-to-Copper Wire Bonding of Cu-Pt-Au-Pd Fine Micro-Alloyed Wires. J. Electron. Mater. 2024, 53, 8048–8065. [CrossRef]
- Chang, Y.T.; Hung, F.Y.; Wu, B.D. Comparison of the Microstructural Characteristics and the Electrothermal Fracture Mechanism of Au-Pd-Coated Copper Wire and Cu-Ti Micro-alloyed Wire. J. Electron. Mater. 2024, 53, 1695–1707. [CrossRef]
- 22. Milad, M.; Zreiba, N.; Elhalouani, F.; Baradai, C. The effect of cold work on structure and properties of AISI 304 stainless steel. *J. Mater. Process. Technol.* **2008**, 203, 80–85. [CrossRef]
- 23. Kumar, A.; Khatirkar, R.K.; Chalapathi, D.; Kumar, G.; Suwas, S. Microstructure and texture development during cold rolling in UNS S32205 and UNS S32760 duplex stainless steels. *Metall. Mater. Trans. A* **2017**, *48*, 2349–2362. [CrossRef]
- 24. Fang, F.; Zhou, L.; Hu, X.; Zhou, X.; Tu, Y.; Xie, Z.; Jiang, J. Microstructure and mechanical properties of cold-drawn pearlitic wires affect by inherited texture. *Mater. Des.* **2015**, *79*, 60–67. [CrossRef]
- 25. Chae, H.; Huang, E.W.; Woo, W.; Kang, S.H.; Jain, J.; An, K.; Lee, S.Y. Unravelling thermal history during additive manufacturing of martensitic stainless steel. *J. Alloys Compd.* **2021**, *857*, 157555. [CrossRef]
- 26. Skvortsov, A.A.; Zuev, S.M.; Koryachko, M.V. Contact melting of aluminum-silicon structures under conditions of thermal shock. *Key Eng. Mater.* **2018**, *771*, 118–123. [CrossRef]
- 27. Islam, M.M.; Couvant, T.; Marcus, P.; Diawara, B. Stress concentration in the bulk Cr2O3: Effects of temperature and point defects. *J. Chem.* **2017**, 2017, 7039436. [CrossRef]
- 28. Padilha, A.F.; Rios, P.R. Decomposition of Austenite in Austenitic Stainless Steels. ISIJ Int. 2002, 42, 325–337. [CrossRef]
- 29. Walker, D.J.; Honeycombe, R.W.K. Effects of deformation on decomposition of austenite: Part II–Carbide precipitation. *Met. Sci.* **1980**, *14*, 184–188. [CrossRef]
- 30. Zhang, Y.; Zou, D.; Li, Y.; Wang, Y.; Zhang, W.; Zhang, X. Effect of Al content on the high-temperature oxidation behavior of 18Cr–Al–Si ferritic heat-resistant stainless steel. *J. Mater. Res. Technol.* **2021**, *11*, 1730–1740. [CrossRef]
- 31. Xu, X.; Zhang, X.; Chen, G.; Lu, Z. Improvement of high-temperature oxidation resistance and strength in alumina-forming austenitic stainless steels. *Mater. Lett.* **2011**, *65*, 3285–3288. [CrossRef]
- 32. Blonde, R.J.P. Austenite Stability in TRIP Steels Studied by Synchrotron Radiation. Ph.D. Dissertation, Eindhoven University of Technology, Eindhoven, The Netherlands, 2014.
- 33. Tao, H.; Zhou, C.; Hong, Y.; Zheng, Y.; Zhang, K.; Zheng, J.; Zhang, L. Influence of Warm Predeformation Temperature on the Corrosion Property of Type 304 Austenitic Stainless Steel. *J. Mater. Eng. Perform.* **2020**, 29, 4515–4528. [CrossRef]
- 34. Miyajima, Y.; Komatsu, S.Y.; Mitsuhara, M.; Hata, S.; Nakashima, H.; Tsuji, N. Change in electrical resistivity of commercial purity aluminium severely plastic deformed. *Philos. Mag.* **2010**, *90*, 4475–4488. [CrossRef]
- 35. Sunderland, K.J.; Slavin, A.J. Thermal decomposition of the (15×3) R14° two-dimensional carbide on the W (110) surface. *Surf. Sci.* **1990**, 233, 89–96. [CrossRef]
- 36. Byun, T.S.; Hashimoto, N.; Farrell, K. Temperature dependence of strain hardening and plastic instability behaviors in austenitic stainless steels. *Acta Mater.* **2004**, *52*, 3889–3899. [CrossRef]

Appl. Sci. 2025, 15, 8572 24 of 24

37. Mitchell, T.E.; Voss, D.A.; Butler, E.P. The observation of stress effects during the high temperature oxidation of iron. *J. Mater. Sci.* **1982**, *17*, 1825–1833. [CrossRef]

38. Talonen, J.; Hänninen, H. Formation of shear bands and strain-induced martensite during plastic deformation of metastable austenitic stainless steels. *Acta Mater.* **2007**, *55*, 6108–6118. [CrossRef]

**Disclaimer/Publisher's Note:** The statements, opinions and data contained in all publications are solely those of the individual author(s) and contributor(s) and not of MDPI and/or the editor(s). MDPI and/or the editor(s) disclaim responsibility for any injury to people or property resulting from any ideas, methods, instructions or products referred to in the content.